Characterization of soot produced by the Mini Inverted Soot Generator with an atmospheric simulation chamber

Virginia Vernocchi[1,2], *Marco Brunoldi*[1,2], *Silvia G. Danelli*[1,2], *Franco Parodi*[2], *Paolo Prati*[1,2], *Dario Massabò*[1,2,*]

[1]*Dipartimento di Fisica - Università di Genova, via Dodecaneso 33, 16146, Genova (Italy)*
[2]*INFN – Sezione di Genova, via Dodecaneso 33, 16146, Genova (Italy)*

**Correspondence to: D. Massabò (massabo@ge.infn.it)*

ABSTRACT

The performance of a Mini-Inverted Soot Generator (MISG) has been investigated at ChAMBRe (Chamber for Aerosol Modelling and Bio-aerosol Research) by studying the properties of soot particles generated by ethylene and propane combustion. This work deepens and expands the existing characterization of the MISG also exploiting an atmospheric simulation chamber (ASC). Differently from previous works, MISG performance has been also tested at different fuel flows and higher global equivalence ratios. MISG exhausts were investigated after their injection inside the atmospheric simulation chamber: this is another novelty of this work. Starting from an extensive classification of combustion conditions and resulting flame shapes, the MISG exhaust was characterized in terms of concentration of emitted particles and gases, particle size distribution and optical properties. Soot particles were also collected on quartz fibre filters and then analysed by optical and thermal-optical techniques, to measure the spectral dependence of the absorption coefficient b_abs, and their composition in terms of Elemental and Organic Carbon (EC and OC). Significant differences could be observed when the MISG is fuelled with ethylene and propane in terms of particle size: in particular, the production of super-micrometric aggregates was observed for ethylene combustion. With equal combustion conditions, ethylene produced higher number concentration of particles and smaller mode diameters. Soot particles produced by propane combustion resulted in higher EC:TC ratios and they were more light absorbing than particles generated by ethylene combustion. Values of the Mass Absorption Cross Section (MAC) and of the Angstrom Absorption Exponent (AAE) turned out to be compatible with the literature, even if with some specific differences. The comprehensive characterization of the MISG soot particles is an important piece of information to design and perform experiments in atmospheric simulation chambers. Particles with well-known properties can be used, for example, to investigate the possible interactions between soot and other atmospheric pollutants, the effects of meteorological variables on soot properties and the oxidative and toxicological potential of soot particles.

1. Introduction

"Soot" refers to combustion-generated carbonaceous particles that are a by-product of incomplete combustion of fossil fuels and/or biomass burning (Nordmann et al., 2013; Moore et al., 2014). When investigated by optical techniques, soot particles are generally referred as Black Carbon, BC (Petzold et al. 2013) while the result of thermal - optical characterizations is referred as Elemental Carbon, EC, (Bond and Bergstrom, 2006). However, both BC and EC are defined in operative terms that do not identify the same compounds (Massabò and Prati, 2021) and often produce non-negligible differences in concentration values.

Soot particles constitute an important fraction of anthropogenic particulate matter (PM) especially in urban environments (Weijer et al. 2011), and are emitted by traffic, domestic stoves, industrial chimneys and by any incomplete combustion process. Several works state adverse effects of soot both on climate (Ackerman et al., 2000; Menon et al., 2002; Quinn et al., 2008; Ramanathan and Carmichael, 2008; Bond et al., 2013) and health (Pope et al., 2002; Anenberg et al., 2010; Gan et al., 2011; Cassee et al., 2013; Lelieveld et al., 2015). From the climatic point of view, soot particles absorb the solar radiation, causing a positive radiative forcing: BC is

considered one of the most significant radiative forcing agent, second only to CO_2 (Ramanathan and Carmichael, 2008; Bond et al., 2013). Another positive effect on radiative forcing is related to the darkening of glaciers surface due to the deposition of BC (Skiles et al., 2018). Soot contributes to air pollution also via reactions with several gas species, as NO_2, SO_2 and O_3 (Finlayson-Pitts and Pitts, 2000; Nienow and Roberts, 2006). Effects on health include cardiopulmonary morbidity and mortality (Janssen et al., 2012). Soot particles are suspected to be particularly hazardous to human health, because they are sufficiently small to penetrate the membranes of the respiratory tract and enter the blood circulation or be transported along olfactory nerves into the brain (Nemmar et al., 2002; Oberdörster et al., 2005). The understanding of properties and behaviour of soot particles when they are suspended in the atmosphere is thus necessary to fully assess their adverse effects and the use of proxies with controlled and known properties can be useful. In this context, soot generators are employed as stable sources of soot particles. So far, soot generators have been employed for studies on optical properties (Zhang et al. 2008; Cross et al. 2010; Mamakos et al. 2013; Utry et al. 2014 b; Bescond et al. 2016), instruments calibration (Onasch et al. 2012; Durdina et al. 2016) and several other purposes, such as studies on atmospheric processing of soot particles, characterization of uncoated/coated and fresh/denuded of soot particles (Pagels et al. 2009; Henning et al. 2012; Ghazi et al. 2013; Ghazi and Olfert 2013; Hu et al., 2021). The Inverted-Flame Burner (Stipe et al. 2005) is often considered as an ideal soot source (Moallemi et al., 2019 and references therein), due to its capacity to generate almost pure-EC particles and for the stability of the flame and of its exhaust (Stipe et al. 2005). To such category belongs the Mini-Inverted Soot Generator, MISG (Argonaut Scientific Corp., Edmonton, AB, Canada, Model MISG–2), used in this work.

The MISG can be operated with different fuels: ethylene (Kazemimanesh et al., 2019), propane (Moallemi et al., 2019, Bischof et al, 2019), and theoretically also with ethane or fuel blends with methane and nitrogen, even if, to our knowledge, no literature is available on such configurations. The air to fuel flow ratio can be adjusted to control concentration and size of the generated particles. The maximum reachable concentration declared by the manufacturer is about 10^7 particles cm^{-3}, while particle size ranges from few tens to few hundreds of nm.

The behaviour of soot particles can be efficiently studied in/by ASCs: these are exploratory platforms which allow to study atmospheric processes under controlled conditions, that can be maintained for periods long enough to reproduce realistic environments and to study interactions among their constituents (Finlayson - Pitts and Pitts, 2000; Becker, 2006). ASC experiments are the best compromise between laboratory and field experiments, since they simulate quasi-real situations but without the uncertainties and variability of typical field measurements. Recent examples of ASC applications concern the investigation of the optical properties of mineral dust (Caponi et al., 2017) and wood-burning exhausts (Kumar et al., 2018, Hu et al., 2021).

Coupling the MISG to an ASC makes possible systematic experiments on the properties of soot particles exposed and maintained in different conditions. In this work, we mainly investigated the differences between MISG exhausts produced by ethylene and propane burning. Differently from previous works (Bischof et al., 2019; Kazemimanesh et al., 2019; Moallemi et al., 2019), the MISG has been connected directly to an atmospheric simulation chamber; performance has been tested also at different fuel flows and higher global equivalence ratios. The present characterization deepens and expands the existing knowledge on particles and gases produced by this soot generator. The comprehensive characterization of the MISG soot particles is an important piece of information to design the subsequent experiments. Well-characterized soot particles could be used to investigate the effects that atmospheric parameters can have on soot particles, and to study the interactions between soot particles and other pollutants.

2. Materials and methods

2.1 Mini-Inverted Soot Generator

The MISG, introduced by Kazemimanesh (2019), is a combustion-based soot generator working as an inverted-flame burner (Stipe et al., 2005) where air and fuel flow in an opposite direction to the buoyancy force

of the hot exhaust gases. The resulting co-flow diffusion flame is more stable thanks to a reduced flickering of flame tip (Kirchstetter & Novakov, 2007; Stipe et al., 2005) and consequently the soot particle generation is more stable.

The MISG is fed with air and fuel supplied by specific cylinders: we used both ethylene and propane, two fuels with a well-known capability of producing soot (Kazemimanesh et al., 2019; Moallemi et al., 2019). Air and fuel flow rates are controlled by two mass flow controllers (MFCs, Bronkhorst High-Tech B.V., Ruurlo, Netherlands, Models F-201CV-10K-MGD-22-V and FG-201CV-MGD-22-V-AA-000, respectively) operated via a home-made National Instruments Labview code. The air and fuel flows can be controlled in the range 0-12 lpm (i.e., litres per minute) and 0-200 mlpm (i.e., millilitres per minute), respectively. Differently from other commercial generators, the MISG does not require a third gas (i.e., N_2) used as a carrier (quenching gas) and the air flow is internally split between combustion and dilution of exhaust product. This implies that the ratio of comburent and carrier gas is not controllable, and the user can only adjust the comburent to fuel ratio.

The efficiency of the combustion process can be given in terms of the global equivalence ratio that is the ratio between actual and stoichiometric fuel-to-air ratio:

$$\varphi = \frac{(m_F/\, m_A)}{(m_F/\, m_A)_{st}} \qquad \text{Eq.1}$$

where:

(m_F/m_A): actual fuel-to-air ratio;

$(m_F/m_A)_{st}$: stoichiometric fuel-to-air ratio.

The fuel-to-air ratio is calculated as the opposite of the air-to-fuel ratio (AFR) that is the ratio between air and fuel masses. The stoichiometric AFR value is 15.64 (inverse value = 0.064) and 14.75 (inverse value = 0.068), for propane and ethylene, respectively.

The flame is classified as fuel-rich and fuel-lean when $\phi > 1$ and $\phi < 1$, respectively. Mamakos (2013) reported that low fuel-to-air ratios (i.e., $\phi < 1$) generate particles with a large fraction of EC while semi-volatile organics are generated by high fuel-to-air ratios (i.e., $\phi > 1$). In this work, fuel-lean conditions were investigated only.

Since the combustion process can produce flame shapes having different characteristics, we first explored the range of combustion flows from 2 to 10 lpm, in 0.5 lpm steps, and from 30 to 100 mlpm, in 5 mlpm steps, respectively for air and fuel. Flame types can be distinguished (Kazemimanesh et al., 2019; Moallemi et al., 2019) as:

- *Closed tip* flame (Fig. 1.a), which generates low concentrations of soot particles (i.e., around 10^3 # cm^{-3}), generally forming particle aggregates at the fuel tube nozzle.
- *Partially Open tip* flame (Fig. 1.b), the transition between *Open* and *Closed tip*.
- *Open tip* flame (Fig. 1.c), which generates high concentrations of soot particles (i.e., > 10^5 # cm^{-3}).
- Asymmetric flame, which shows a large variability (very short, flickering, etc) and can form particle aggregates at the fuel tube nozzle.
- *Curled Base* flame (Fig. 1.d), a particular shape of the asymmetric flames that can also form particles aggregates at the fuel tube nozzle.

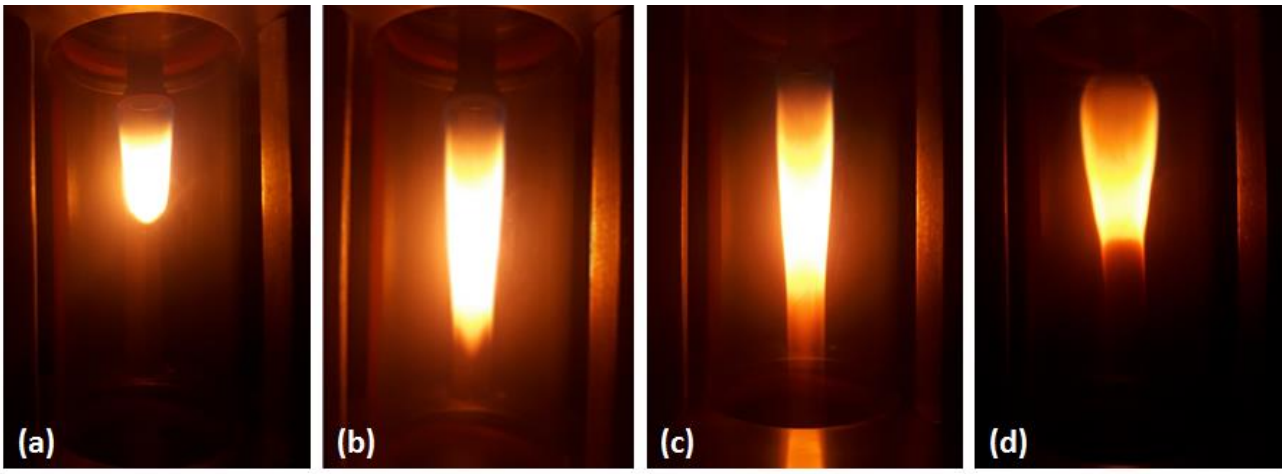

Figure 1: Examples of different flame shapes: (a) Closed tip, (b) Open tip, (c) Partially Open tip, (d) Curled base flame.

By the flames observation, we selected the more interesting combustion conditions (i.e., *Open tip* flames) to perform the characterization experiments. We focused on *Open tip* flames because it is the flame that generates higher concentrations of soot particles. Operative conditions selected for propane and ethylene combustion are reported in Tables 1 and 2: we maintained the same air flow and global equivalence ratio with both the fuels.

Table 1: Combustion parameters and flame shapes selected for propane.

PROPANE			
AIR flow [lpm]	**FUEL flow [mlpm]**	**Global Equivalence Ratio**	**Flame shape**
7	70	0.244	Partially Open Tip
7	75	0.261	Open Tip
7	80	0.278	Open Tip
7	85	0.296	Open Tip
8	70	0.213	Partially Open Tip
8	75	0.228	Open Tip
8	80	0.244	Open Tip
8	85	0.259	Open Tip

146 *Table 2: Combustion parameters and flame shapes selected for ethylene.*

ETHYLENE			
AIR flow [lpm]	**FUEL flow [mlpm]**	**Global Equivalence Ratio**	**Flame shape**
7	118	0.244	Partially Open Tip
7	127	0.261	Open Tip
7	135	0.278	Open Tip
7	144	0.296	Open Tip
8	118	0.213	Partially Open Tip
8	127	0.228	Open Tip
8	135	0.244	Open Tip
8	144	0.259	Open Tip

147

148

149 **2.2 Chamber setup**

150 Experiments took place at the ChAMBRe (Chamber for Aerosol Modelling and Bio-aerosol Research)
151 facility (Massabò et al., 2018; Danelli et al., 2021) located at the Physics Department of the University of
152 Genoa.
153 ChAMBRe is a stainless-steel chamber, with a volume of about 2.2 m^3. Inside the chamber, relative
154 humidity, temperature, and pressure are continuously monitored by a HMT334 Vaisala® Humicap®
155 transmitter and a MKS Instruments 910 DualTrans™ transducer, respectively. Two gas analyzers from
156 Environnement SA, continuously monitored the concentration of NO/NO_2 (model: AC32e), and CO/CO_2
157 (model: CO12e) inside the chamber or, alternatively, in the laboratory. The mixing of gas and aerosol species
158 is favoured by a fan installed in the bottom of the chamber: mixing time for gaseous species is of about 180 s
159 with a fan rotating speed of 1.6 revolutions per second. A composite pumping system (rotary pump TRIVAC®
160 D65B, Leybold Vacuum, root pump RUVAC WAU 251, Leybold Vacuum and Leybold Turbovac 1000)
161 allows to evacuate the internal volume down to 10^{-5} mbar; in this way ChAMBRe is cleaned before each
162 experiment. Before and during the experiments, ambient air enters the chamber throughout a 5-stage
163 filtering/purifying inlet (including a HEPA filter, model: PFIHE842, NW25/40 Inlet/Outlet – 25/55 SCFM,
164 99.97 % efficient at 0.3 μm). The whole set-up is managed by a custom NI Labview SCADA (Supervisory
165 Control And Data Acquisition).
166 The layout of the experimental configuration adopted for the MISG characterization is shown in Fig. 2.
167 The MISG was warmed for about 45 minutes before injecting soot particles inside the chamber. Injection
168 of soot particles inside ChAMBRe lasted 2 or 3 minutes, depending on the soot concentration required for each
169 experiment. We performed some fluid dynamic evaluations with the Particle Loss Calculator software tool
170 (PLC; von der Weiden et al., 2009). The connection between MISG and ChAMBRe was made by Swagelok
171 adaptors (size ¾") and ISO-K flanges (16 mm diameter) to avoid any possible leak; the length of the line was
172 65 cm. The geometry of our experimental setup, combined with particle size and used flow rates, resulted in

particle losses lower than 0.1 % in the dimensional range of 80-2000 nm. All the experiments were performed at atmospheric pressure, 19° < T< 21 °C and R.H. < 50 %.

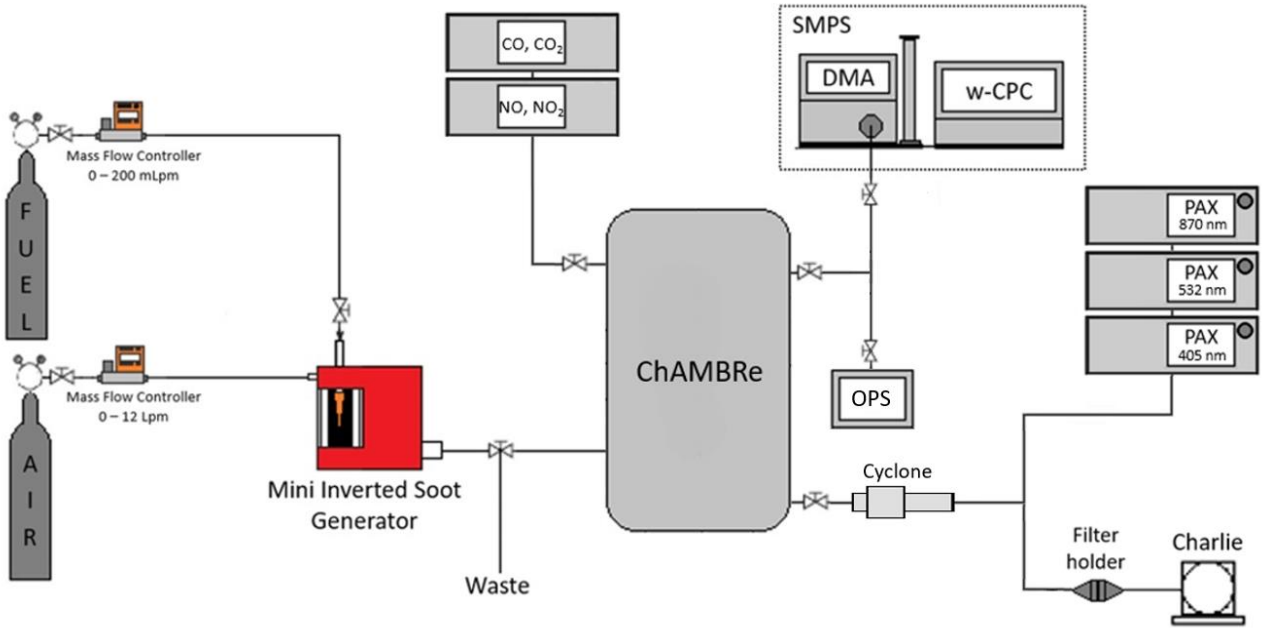

Figure 2: Layout of the MISG set-up at ChAMBRe.

2.3 Size distribution measurements

Particle concentration and size distribution inside the chamber were measured by a scanning mobility particle sizer (SMPS, TSI Inc., Shoreview, MN, USA, Model 3938), composed by a differential mobility analyzer (DMA, TSI Inc., Shoreview, MN, USA, Model 3081A) and a water condensation particle counter (w-CPC, TSI Inc., Shoreview, MN, USA, Model 3789). The water-CPC is filled using technical demineralized water (Conductivity (20°C), max. 1.5 µS/cm; VWR Chemicals INTERNATIONAL S.R.L.). The SMPS was set to measure particles with mobility diameter from 34 nm to 649 nm; aerosol sample and sheath airflow rates were fixed at 0.17 lpm and 1.60 lpm, respectively, while the scanning period for each cycle was 70 s. The DMA unit integrates an impactor with an orifice of 0.0508 cm, resulting in cut-off capability at 50 % of 940 nm, useful to exclude all the particles larger than this size to enter in the column. Frequent cleaning of this part was necessary to ensure proper operation and avoid clogging; at the end of each experiment, the whole impactor system was cleaned using compressed air and isopropyl alcohol.

We corrected diffusion losses in the instrument by using the option included in the instrument software; size distributions were not corrected for multiple charges effects through the TSI proprietary software (Aerosol Instrument Manager, Version 11-0-1). An example of comparison between size distribution corrected and uncorrected by the multiple charge correction algorithm is shown in the Supplementary (see Fig. S.1).

Among the other chamber instruments, an Optical Particle Sizer (OPS, TSI Inc., Shoreview, MN, USA, Model 3330) was used for short times to spot the particle size distribution in the range 0.3-10 µm.

2.4 Online optical measurements

Three photoacoustic extinction-meters (PAXs, Droplet Measurement Technologies, Boulder, CO, USA) were deployed, providing the online determination of the soot particles absorption coefficients at λ = 870, 532

and 405 nm. PAXs are constituted by a measurement cell where aerosol optical properties are measured by two different mechanisms (https://www.dropletmeasurement.com/ PAX Operator Manual). The sample flow rate (1 lpm) is split in two different sectors of the cell, both crossed at the same time by the light of a modulated laser diode. In the absorption sector, soot particles absorb light and release acoustic waves, which are then detected by an ultra-sensitive microphone. The intensity of the acoustic signal is interpreted to infer the particle absorption coefficient. In the other sector, a wide-angle reciprocal nephelometer measures the scattering coefficient instead. It is noteworthy that no correction for the truncation angle is applied by the manufacturer: this can lead to substantial underestimation of the scattering coefficient, which generally grows as the particle size increases and the single scattering albedo (SSA) approaches unity. Few papers in literature deal with the correction for truncation errors in nephelometer measurements (Bond et al., 2009, Modini et al, 2021) for highly absorbing particles: little is known on the dependency of scattering phase function on the particle morphology and how this might impact truncation. However, since particles produced by soot generators have dimensions generally lower than 1 μm and SSA values lower than 0.3 (Moallemi et al., 2019), we disregarded this issue. At the time of the experiments, the three PAXs had been just calibrated by the manufacturer.

In some experiments, soot concentration inside the chamber was too high to be measured directly by PAXs; and a diluter (eDiluter Pro, Dekati Ltd., Kangasala, Finland) was deployed. Dry air from a cylinder was merged prior to the PAXs inlet with dilution factor 1:100. Tests performed with and without the diluter demonstrated a substantial reproducibility of the optical properties measured by the PAXs when the proper dilution factor is considered.

2.5 Offline analysis

Soot particles were also collected on pre-fired 47 mm diameter quartz fibre filters (Pallflex Tissuquartz 2500 QAO-UP) held in a stainless-steel filter holder to allow additional offline analysis. The sampling started when stable gas and particle concentration values were reached inside the chamber (i.e., about 3 minutes - corresponding to the chamber mixing time - after the MISG switching off): for each working condition three filters with different loadings were obtained by a low-volume sampler (TECORA – Charlie HV) working at a fixed sampling flow (i.e., 10 lpm during experiments without cyclone and 13.67 lpm during experiments with cyclone).

For each sample, the EC and OC mass concentration was determined by thermal-optical transmittance analysis (TOT) using a Sunlab Sunset EC/OC analyzer and the NIOSH5040 protocol (NIOSH, 1999), corrected for temperature offsets. We also performed some tests adding a backup filter during the sampling to determine the volatile fraction of OC.

Prior to EC/OC determination, particle-loaded filters were analyzed by the Multi-Wavelength Absorbance Analyzer (MWAA, Massabò et al., 2013 and 2015), a laboratory instrument for the offline direct quantification of the aerosol absorption coefficients at five different wavelengths (λ = 850, 635, 532, 405 and 375 nm). Such features have been previously exploited in the frame of several field campaigns in urban and rural sites (Scerri et al., 2018; Massabo et al, 2019; Massabo et al, 2020; Moschos et al., 2021), as well as in remote sites (Massabo et al., 2016; Saturno et al., 2017; Baccolo et al., 2021).

2.6 Cyclone experiments

Soot aggregates are also generated by the MISG. Kazemimanesh (2019) retrieved super-aggregates larger than 2 μm for ethylene combustion while Moallemi (2019) showed aggregate structures larger than 1 μm with propane. On this basis, confirmed by some short checks by the OPS, we replicated each experiment (see Sect. 2.1) both without and with a cyclone (PM1 Sharp Cut Cyclone - SCC 2.229, MesaLabs, Lakewood, CO, USA) inserted upstream the PAXs and filters sampler (Fig. 2). The cyclone has a cut-off of 1 μm at a nominal flow of 16.66 lpm.

3. Results and Discussion

3.1 Characterization tests

The categories of flame shape observed in the range of air and fuel flows discussed in sect. 2.1.2 are summarized in Supplementary (see Tables S.1 and S.2), for propane and ethylene respectively. The MISG characterization with propane has been previously published (Moallemi et al., 2019) and we used it as a reference. Fuel flows higher than 85 mlpm were not investigated due to instrumental limitation. A similar characterization with ethylene also exists but it only partly covers the flow ranges explored in the present work. We got some differences especially in the transition range to *Open tip* flames, probably due to the different setups. In addition, the subjectivity of the visual determination, that is user dependent, can lead to differences. It is noteworthy that no correlation could be found between the global equivalence ratio (ϕ) and the shape of the corresponding flame. This means that the fundamental parameter of the combustion process can not be used to predict the flame shape.

The repeatability and stability of the MISG emissions were investigated for all the combustion conditions listed in Table 1 and 2, in terms of number concentration and size distribution of the generated soot particles. Different combustion conditions were selected, and four experiments were performed for each combination of air and fuel flows. We chose to keep fixed the air flow to observe the differences produced by different fuel flows that correspond to different flame shapes (i.e., *Partially Open tip* or *Open tip*). In each test, we recorded the values of total particle number concentration, peak concentration, and mode diameter. The repeatability was calculated as the percentage ratio between standard deviation and mean value (i.e., the relative standard deviation) of identical repeated experiments. With propane, mode reproducibility turned out to be 6 %, while total concentration and peak concentration showed a 16 % repeatability. With ethylene, the repeatability was 4 % and 10 %, respectively for mode and total/peak concentration. In addition, we monitored the combustion gases: CO_2 and NO concentration varied by about 2 % and 3 %, respectively with propane and ethylene.

3.2 Comparison between propane and ethylene exhausts

Previous works investigated the exhausts of MISG fuelled by ethylene (Kazemimanesh et al., 2019) and propane (Moallemi et al., 2019). We expand here to a detailed comparison between the two fuels, focusing on ASC experiments. In addition, we reproduced some of the conditions investigated in the previous works obtaining a good agreement for the mode diameter and SSA figures (see §3 in Supplementary for details).

3.2.1 Size distribution

The mean size distributions observed at ChAMBre are given in Fig. 3, for all the selected operative conditions. Data were acquired starting 3 minutes (i.e., after the chamber mixing time) after the MISG switching off, for a specific time interval (i.e., 4 to 10 minutes). All the curves are normalized to the same injection time (i.e., 3 min of injection inside the chamber).

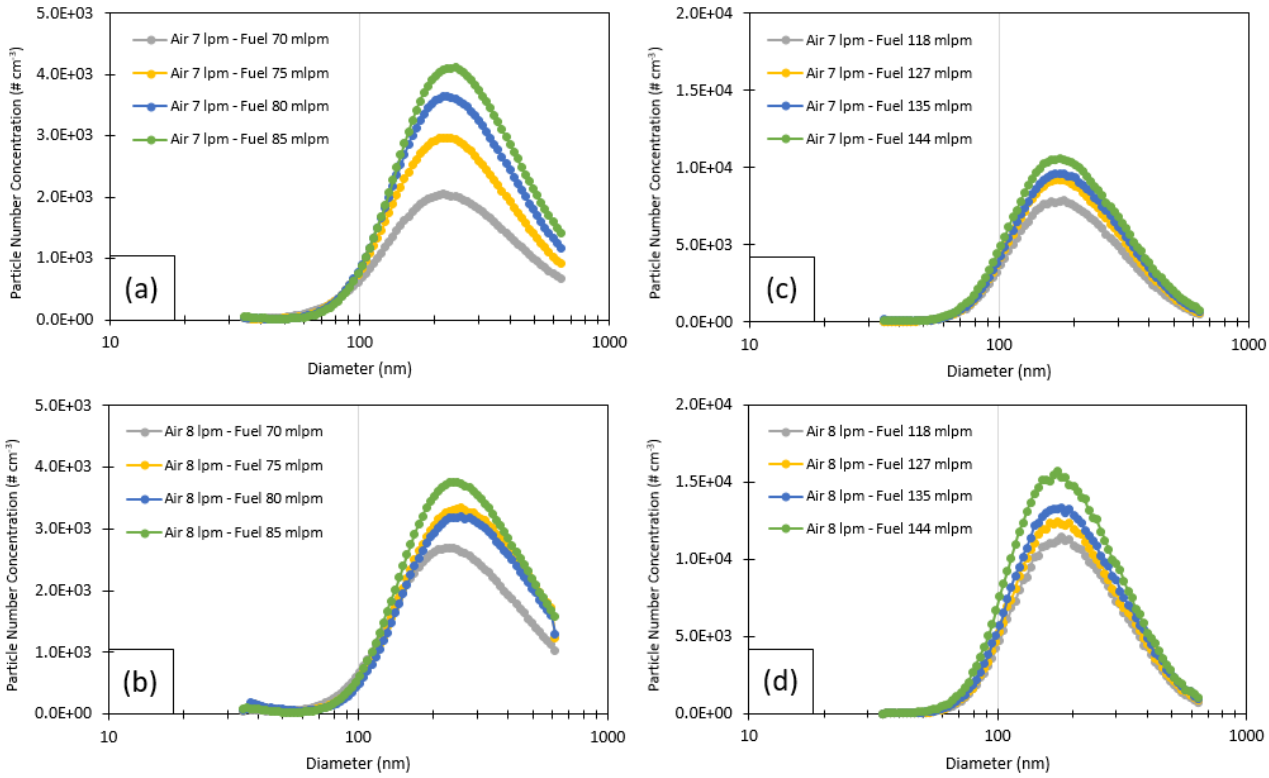

Figure 3: Mean size distributions measured by SMPS. MISG was fuelled with propane (a) and (b) panels and ethylene (c) and (d) with the air and fuel flows indicated in the plots frame.

For a better comparison of different experiments, particle concentration values were normalized to the maximum recorded in the whole set of tests and therefore varied in the 0-1 range. Fig. 4 shows the result for the total particle number concentration. We can notice that:

- At fixed air flow, the particle number concentration increases with the fuel flow (i.e., with the global equivalence ratio).
- In the same combustion conditions (i.e., same air flow and same global equivalence ratio), ethylene generates more particles than propane.
- With ethylene and at fixed fuel flow, the particle number concentration increases with the air flow. The same holds in some cases with propane but with much smaller variations.

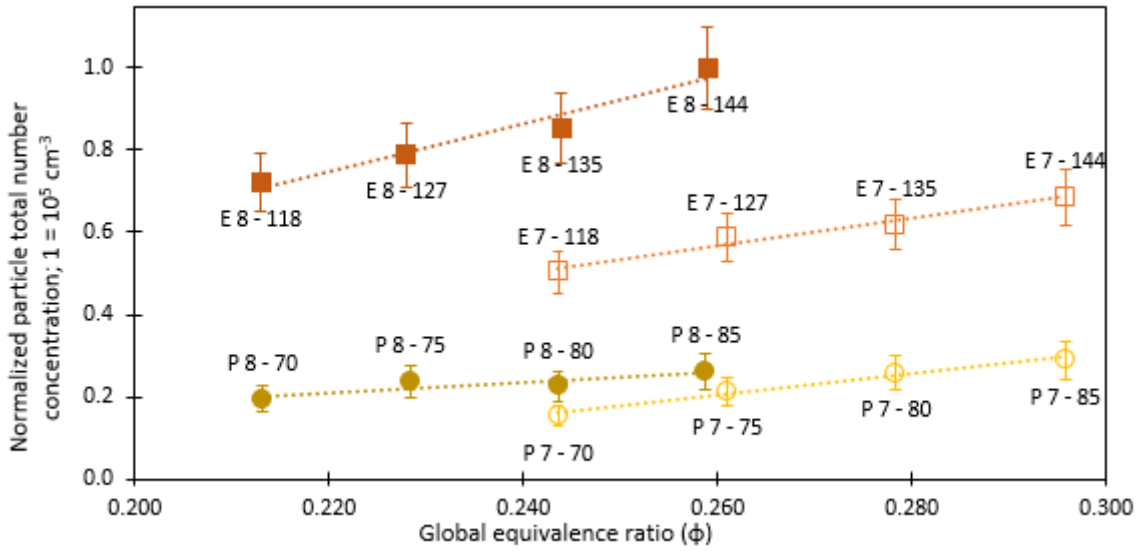

Figure 4: Particle number concentration vs the global equivalence ratio. Values are normalized to the highest of the whole set. Each point is labelled by E or P (ethylene or propane) and a pair of numbers indicating air and fuel flow rate, respectively in lpm and mlpm. Dotted lines aim to facilitate the reader eye.

A similar comparison is shown in Fig. 5 for the particle mode diameter: while the values are basically constant for ethylene, the mode diameter with propane slightly increases with air flow (at fixed fuel flow). Furthermore, at each ϕ value, propane generated particles bigger than ethylene.

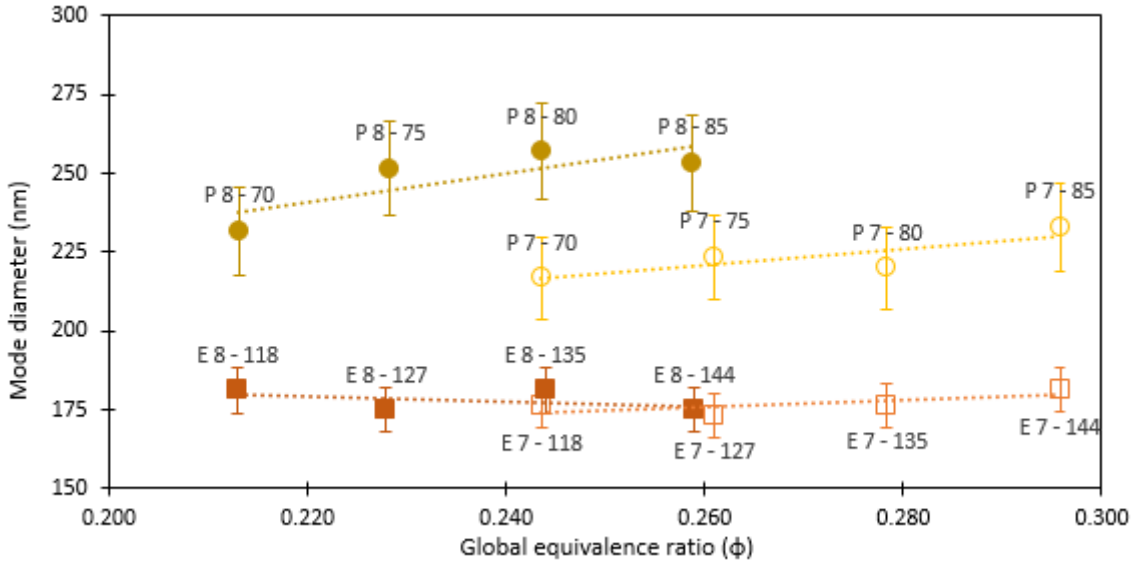

Figure 5: Mode diameter versus the global equivalence ratio. Each point is indicated by E or P (ethylene or propane) and a pair of numbers indicating air and fuel flow rate, respectively in lpm and mlpm. Dotted lines aim to facilitate the reader eye.

Even if the direct comparison between our findings and results from previous works (Bischof et al., 2019; Kazemimanesh et al., 2019; and Moallemi et al., 2019) are not directly comparable (since feeding flows and global equivalence ratios are different), some similarities can be identified. Previous works observed that by increasing the fuel flow, the particle number concentration increases too, that is in agreement with what we observed for both the fuels. In addition, Bischof (2019) reported that with propane the particle mode diameter did not depend on the global equivalence ratio; we observed this behaviour for ethylene instead.

Kazemimanesh (2019) showed a clear increase in mode diameter, corresponding to an increase of fuel flow rate, that reached a quite constant value (i.e., around 240-270 nm) for ethylene. This trend differs from our observations, since the mode diameter in our case turned out to be quite stable at about 175 nm independently on feeding flows. This difference is probably due to the global equivalence ratios used: while in (Kazemimanesh et al., 2019) global equivalence ratios are lower than 0.206, in our case they are higher than 0.213. In (Moallemi et al., 2019), instead, they observed an opposite behaviour for mode diameters: they retrieved that at fixed fuel flow, a higher air flow produced a slight decrease of the mode diameter. Both (Moallemi et al., 2019) and (Bischof et al., 2019) measured mode diameters < 200 nm, but they used different combustion conditions (i.e., lower global equivalence ratios resulting from higher air flow or lower fuel flow). We can conclude that, as expected, global equivalence ratio is the principal parameter affecting size distributions of soot particles.

Significant differences between the two fuels emerge when considering the super-micrometric range measured by the OPS: ethylene combustion produced a number of big particles, likely super-aggregates, probably formed in the stagnation plane at the bottom part of the combustion cell (Chakrabarty et al., 2012). This hypothesis was confirmed by dedicated experiments with the setup specifically modified in respect to the basic one (see Supplementary Fig. S.2). Kazemimanesh (2019) also observed the formation of aggregates, even with smaller dimensions (i.e., about 2 μm of maximum Feret diameter). The particle number concentration, normalized to the total particle number concentration, is shown in Fig. 6.a. We calculated the super-micrometric fraction of the total number concentration measured by the OPS with both the fuels (Fig. 6.a): this resulted to be about 3% with ethylene and 0.2% with propane. Particles larger than 4 μm (i.e., optical equivalent diameter) were about 2% with ethylene and totally negligible with propane. Considering the particle mass distribution (see Fig. 6.b), the difference is enhanced: the super-micrometric fraction is about 99% of the total mass concentration with ethylene and 9% only with propane. Particles larger than 4 μm contribute to the total mass (and hence to the soot concentration) for about 98% and 1%, respectively with ethylene and propane.

Anyway, super-aggregates formation by ethylene combustion can be partly reduced by using lower air and fuel flow rates (see Supplementary Fig. S.3 for example).

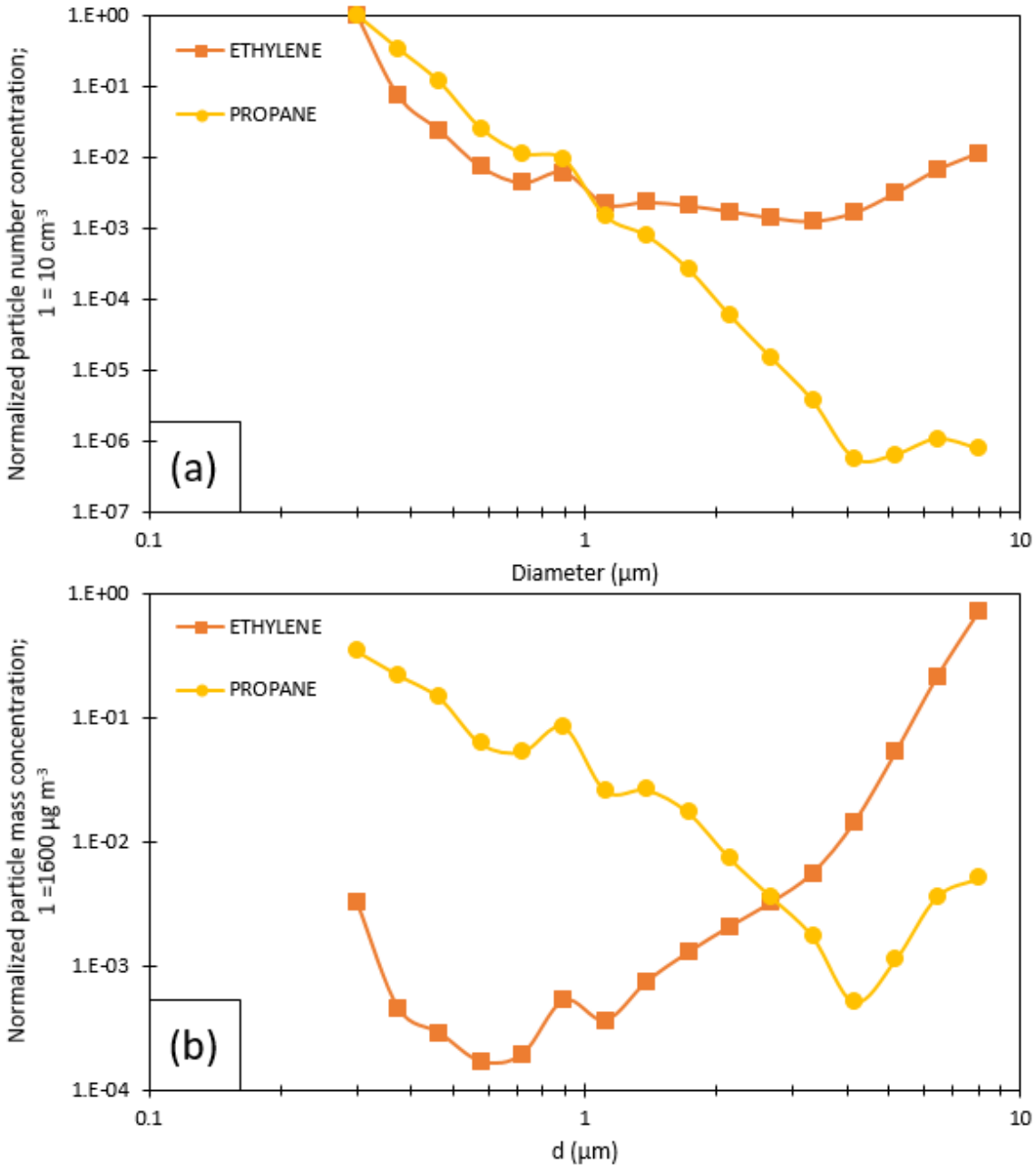

Figure 6: Particle concentration normalized to the total vs. particle diameter, measured by OPS, panel (a) shows number distribution, panel (b) shows mass distribution. MISG was fuelled with 7 lpm of air and 75 mlpm of fuel during propane experiment and 127 mlpm of fuel during ethylene experiment. No cyclone used.

3.2.2 Gaseous exhaust

Gaseous emissions were characterized too, focusing on the most abundant gases i.e., CO_2 and NO. The pattern is similar for both the gases: at fixed air flow rate, gas concentration increased with the fuel flow while no significant differences emerged at fixed fuel flow rate and changing the air flow. At equal operative conditions (i.e., same combustion conditions, injection time and time from the injection), gaseous emissions were higher with ethylene than with propane. With the same normalization introduced in Fig. 3, the CO_2 and NO production are compared in Fig. 7 and 8 for each selected MISG configuration. Maximum values were 360 ppm and 980 ppb, respectively for CO_2 and NO, after 3 minutes of soot injection.

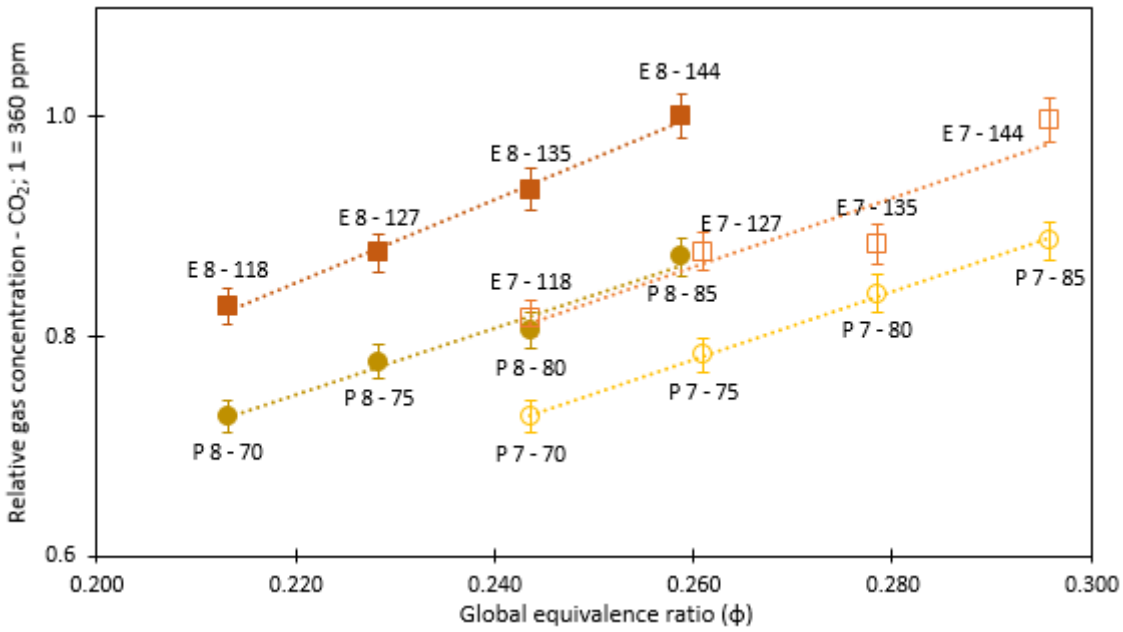

345

346

347 *Figure 7: CO_2 concentration versus the global equivalence ratio. Each value was normalized to the highest of the whole*
348 *set. Data points are labelled by E or P (ethylene or propane) and a pair of numbers indicating air and fuel flow,*
349 *respectively in lpm and mlpm. Dotted lines aim to facilitate the reader eye.*

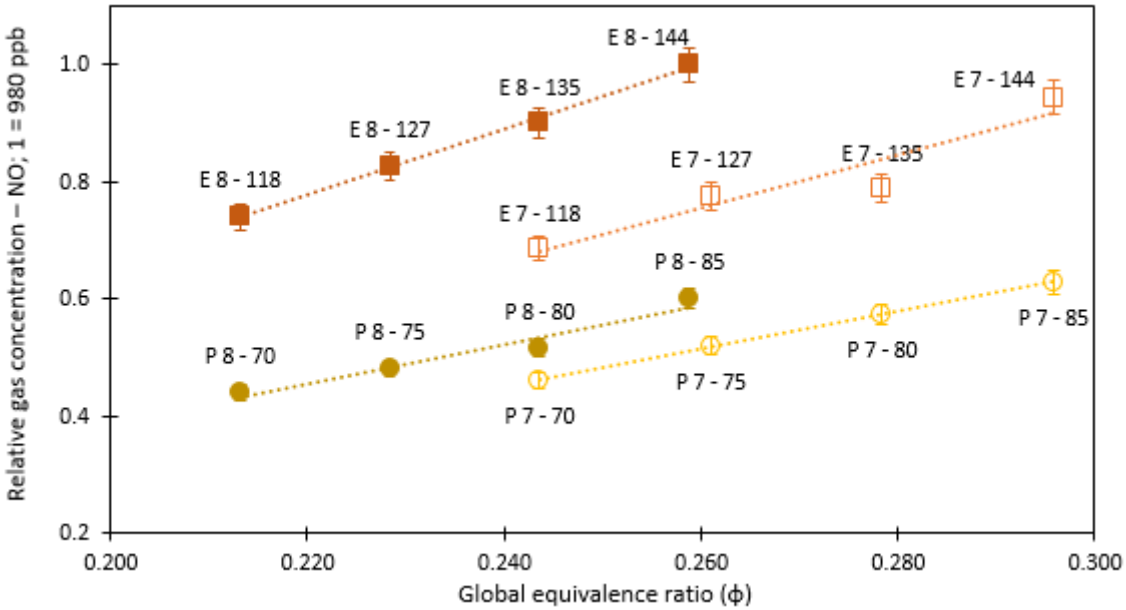

350

351

352 *Figure 8: NO concentration versus the global equivalence ratio. Each value was normalized to the highest of the whole*
353 *set. Data points are labelled by E or P (ethylene or propane) and a pair of numbers indicating air and fuel flow,*
354 *respectively in lpm and mlpm. Dotted lines aim to facilitate the reader eye.*

355 **3.2.3 EC/OC quantification**

The OC/EC composition was quantified by thermal-optical analysis of samples collected on quartz fibre filters during each experiment. EC:TC concentration ratios resulted to be around 0.7 and 0.9 with propane and ethylene, respectively. In addition, the EC:TC concentration ratios increased with the global equivalence ratio. All the results are given in Fig. 9a and 9b, for experiments without and with cyclone, respectively, adopting the same normalization already introduced in Fig. 3. When removing large particles (see Sect 3.2.1), the EC:TC concentration ratio resulted higher with propane (0.83 against 0.79 measured with ethylene). It is worthy to note that with ethylene about 40 % of the EC concentration was associated with particles larger than 1 μm. With both fuels, EC:OC ratios increase with the global equivalence ratios whether the cyclone is present or not, in agreement with (Kazemimanesh et al., 2019) and (Moallemi et al., 2019).

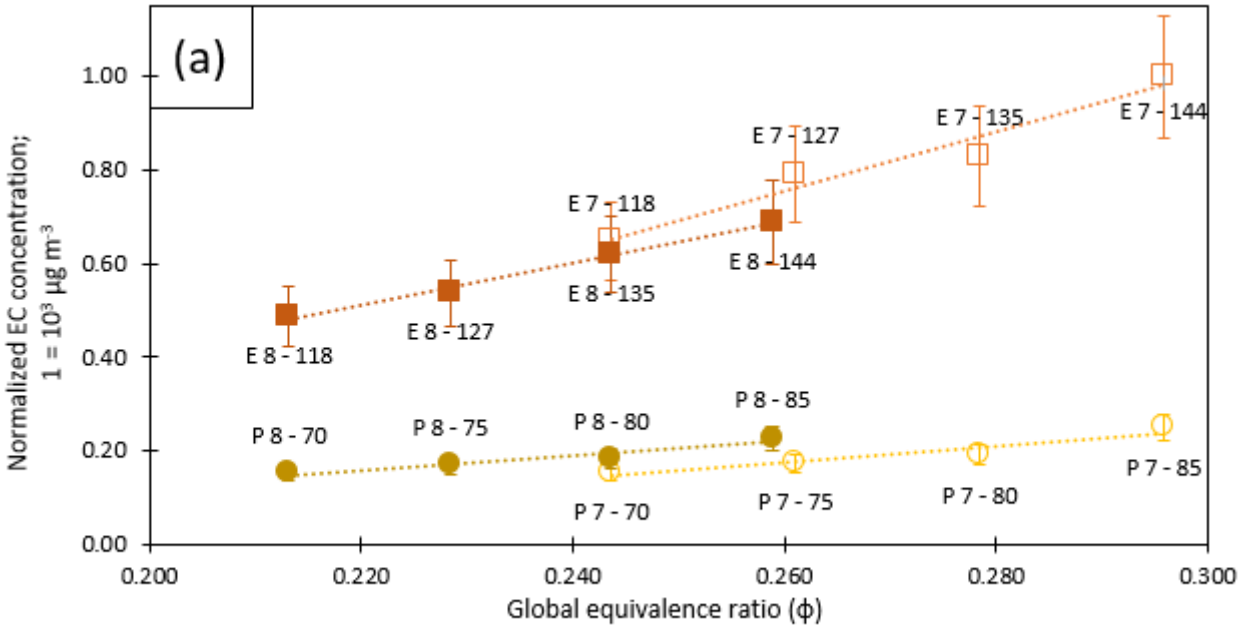

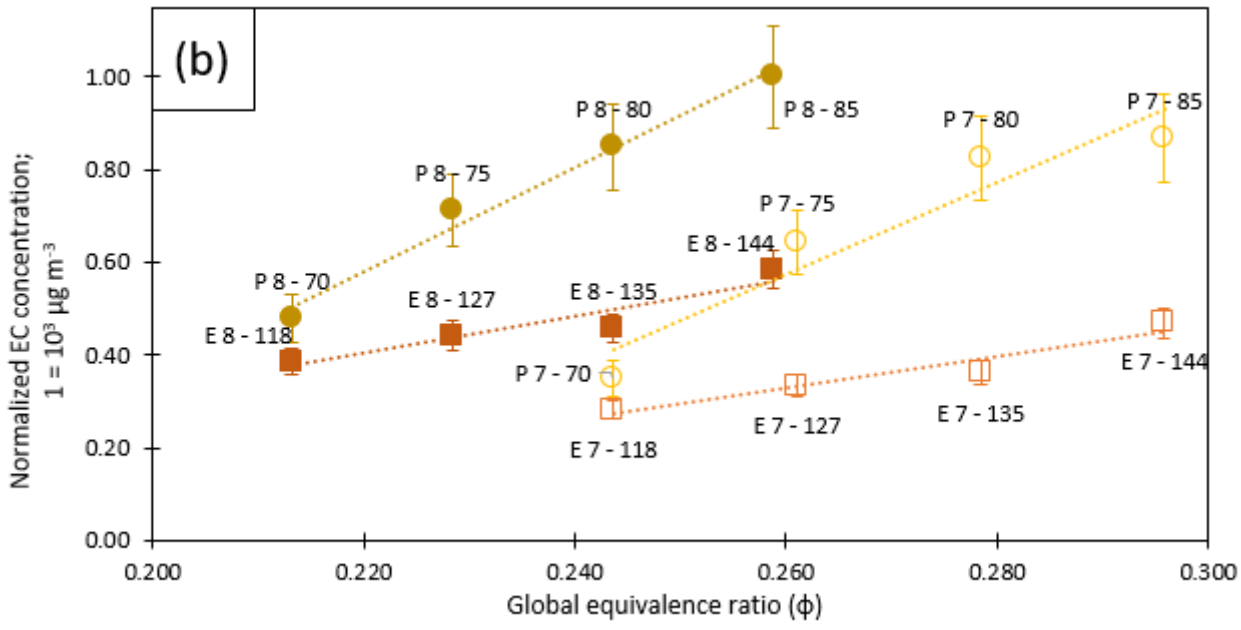

Figure 9: EC mass concentration versus the global equivalence ratio, each value was normalized to the highest of the whole set. Each point is labelled by E or P (ethylene or propane) and a pair of numbers indicating air and fuel flow rate, respectively in lpm and mlpm. (a): no cyclone; (b) cyclone upstream the filter. Dotted lines aim to facilitate the reader eye.

The OC:TC ratio varies from 0.27 for propane to 0.11 for ethylene, without cyclone and 0.20 for ethylene to 0.16 for propane, when the cyclone was used. In each series of experiments (i.e., air flow rate 7 or 8 lpm, ethylene or propane) the OC fraction turned out to be inversely proportional to the fuel flow with a minimum at the lowest fuel flow (i.e., 70 lpm with propane and 118 lpm with ethylene). This is likely due to the shape of the flame: flames generated by the lowest fuel flow conditions are *Partially Open tip*, with less capability to generate soot particles and hence EC; so that the EC:TC ratio results lower.

We also performed some tests to determine the volatile fraction of OC. The OC concentration values measured on backup filters showed high variability, but they were compatible with those on not-sampled filters. We analysed 13 blank filters from different bunches and the average concentration of OC resulted $<OC> = 0.5 \pm 0.2$ μg cm^{-2} while OC concentration on backup filters was $<OC_{BF}> = 0.6 \pm 0.2$ μg cm^{-2} Since the average OC concentration on the corresponding main filters was 1.4 ± 0.7 μg cm^{-2} and the average EC concentration collected on this subset of filter was 12.3 ± 0.2 μg cm^{-2}, the volatile fraction phase can be considered negligible. A relationship between OC concentration on the backup filter and the global equivalence ratio was instead reported in (Kazemimanesh et al., 2019). Actually, in that study the range of investigated global equivalence ratio values was $0.129 < \phi < 0.186$ to be compared $\phi > 0.210$ adopted in this work.

3.2.4 Optical properties

The optical properties of the MISG aerosol were determined in terms of the absorption coefficient (b_abs; i.e. the absorbance per unit length) (Massabò and Prati, 2021). The b_abs definition applies both to measurements directly performed on the aerosol dispersed in the atmosphere (by PAXs, in this work) and to off-line analyses on aerosol sampled on filters (by MWAA, in this work), provided a proper data reduction is adopted (Massabò and Prati, 2021; and references therein).

The online measured b_abs values were normalized to the total particle number concentration inside ChAMBRe reached in each single experiment. At each wavelength, the b_abs values did not show any dependence on the global equivalence ratio, with the propane producing particles more absorbent than ethylene (see Supplementary Fig. S.4 and S.5, for the experiments without and with cyclone, respectively). Similar results were obtained even for experiments without cyclone and for the b_abs values measured by the MWAA. Optical properties such as absorption depend on several parameters, mainly composition, mixing state, aging, and size. Considering all the experiments reported in this work, no differences in composition can be expected, since only EC particles were present: this means that differences in absorption cannot depend on particle composition. Also mixing state and aging cannot explain this difference: soot inside the chamber was fresh. We can explain the higher light absorbing capability of propane by considering differences in: size distributions (see Figs. 3-5) and morphology/density of the particles produced by the burning of the two different fuels.

In the literature, only data for the IR-PAX in terms of Single Scattering Albedo (SSA) for propane soot are reported. SSA(IR) values, measured during propane experiments, in our work varied from 0.15 to 0.18, in agreement with those obtained by (Moallemi et al., 2019), which ranged from 0.15 to 0.25.

The b_abs values, together with the EC concentration measured on the filter sampled during each single experiment, can be used to retrieve the Mass Absorption Coefficient (MAC) of the produced aerosol, through the relation:

$$b\_abs(\lambda) = MAC * [EC] \qquad \text{Eq. 2}$$

where:

b_abs [Mm^{-1}]: absorption coefficient
MAC [$m^2\ g^{-1}$]: Mass Absorption Coefficient
EC [$\mu g\ m^{-3}$]: Elemental Carbon concentration

The b_abs values were calculated directly online by the PAXs and offline by the MWAA analysis, performed at five wavelengths on the sampled filters (see Sect. 2.5). This gave the possibility to extend the characterization of the MISG and to compare two optical analyses on the same carbonaceous aerosol. Since experiments were repeated with two different setups (i.e., with and without the cyclone) and two different fuels (propane and ethylene), four different particle populations can be compared. The comparison was carried out at the three wavelengths (nearly) common to PAXs and MWAA (i.e., λ = 870/850, 532 and 405 nm). Fig 10 shows the comparison at λ = 870/850 nm, while comparison at λ = 532 and 405 nm are reported in Supplementary (see Fig. S.6 and S.7, respectively).We divided the results by fuel, air flow and with/without cyclone. Each point in the plots sums-up the observations at different global equivalence ratio values. All the measured MAC values, including the other two wavelengths available for the MWAA (i.e., 635 and 375 nm) too, are summarized in Table 5.

Table 5: Summary of the measured MAC values, in $m^2\ g^{-1}$.

FUEL	PAX			MWAA				
	870 nm	532 nm	405 nm	850 nm	635 nm	532 nm	405 nm	375 nm
PROPANE	5.30 ± 0.06	8.35 ± 0.08	10.55 ± 0.11	5.22 ± 0.06	7.22 ± 0.09	8.81 ± 0.09	10.55 ± 0.09	10.86 ± 0.12
PROPANE with cyclone	6.27 ± 0.06	10.26 ± 0.06	13.48 ± 0.08	5.32 ± 0.06	7.37 ± 0.07	8.95 ± 0.08	10.91 ± 0.11	11.59 ± 0.14
ETHYLENE	3.28 ± 0.15	4.92 ± 0.19	5.89 ± 0.20	3.78 ± 0.08	5.00 ± 0.09	5.91 ± 0.11	6.90 ± 0.12	7.28 ± 0.14
ETHYLENE with cyclone	5.41 ± 0.08	10.42 ± 0.12	15.74 ± 0.15	5.21 ± 0.06	7.62 ± 0.07	9.53 ± 0.08	12.29 ± 0.10	13.03 ± 0.11

The MWAA analysis at λ = 870 nm (Fig. 10.a) returned compatible MAC values for both propane series (with/without cyclone) and ethylene series with cyclone, while a consistently lower MAC value was found for the ethylene series (worse correlation) without the PM1 cutting. The same picture turned out at the other two wavelengths (see Supplementary Fig. S.6 and S.7). By comparing PAX absorption coefficients and EC concentrations at λ = 870 nm (Fig. 10.b), obtained MAC values are more variable, with similar values only in the case of propane without cyclone and ethylene with cyclone. At λ = 532, in the case of MWAA, similar MAC values have been found for both the propane series, while, for ethylene series, MAC values were slightly higher when cyclone was used and lower when not. Considering the optical data from PAX, a similar MAC for both the fuels was found when the cyclone was present, while it slightly differed in the case of propane without cyclone, and it was much lower in the case of ethylene without cyclone. At λ = 405 nm, the MWAA responses for propane series were still in agreement while the ethylene series showed a higher MAC value when using the cyclone, and a lower MAC value without using it. PAX returned a different MAC value for each of the four conditions. To summarize, if series with cyclone are only considered, MAC values show small differences depending on the fuel, larger in the case of PAXs. The ethylene series without cyclone showed the lowest MAC values of the whole data set: the most likely reason for this difference is the presence of super-micrometric particles (see Sect 3.2.1 and Fig. 6) when the cyclone was not used. With MWAA, the MAC values turned out to be the same in all the runs but the case of the ethylene data collected without the cyclone. With the PAXs analysis, MAC values turned out higher in the series with cyclone, this happened at all the three wavelengths and for both fuels. Since PAXs data showed a higher variability in MAC values, photoacoustic measurements are supposed to be more sensitive to particle size than filter based MWAA analysis.

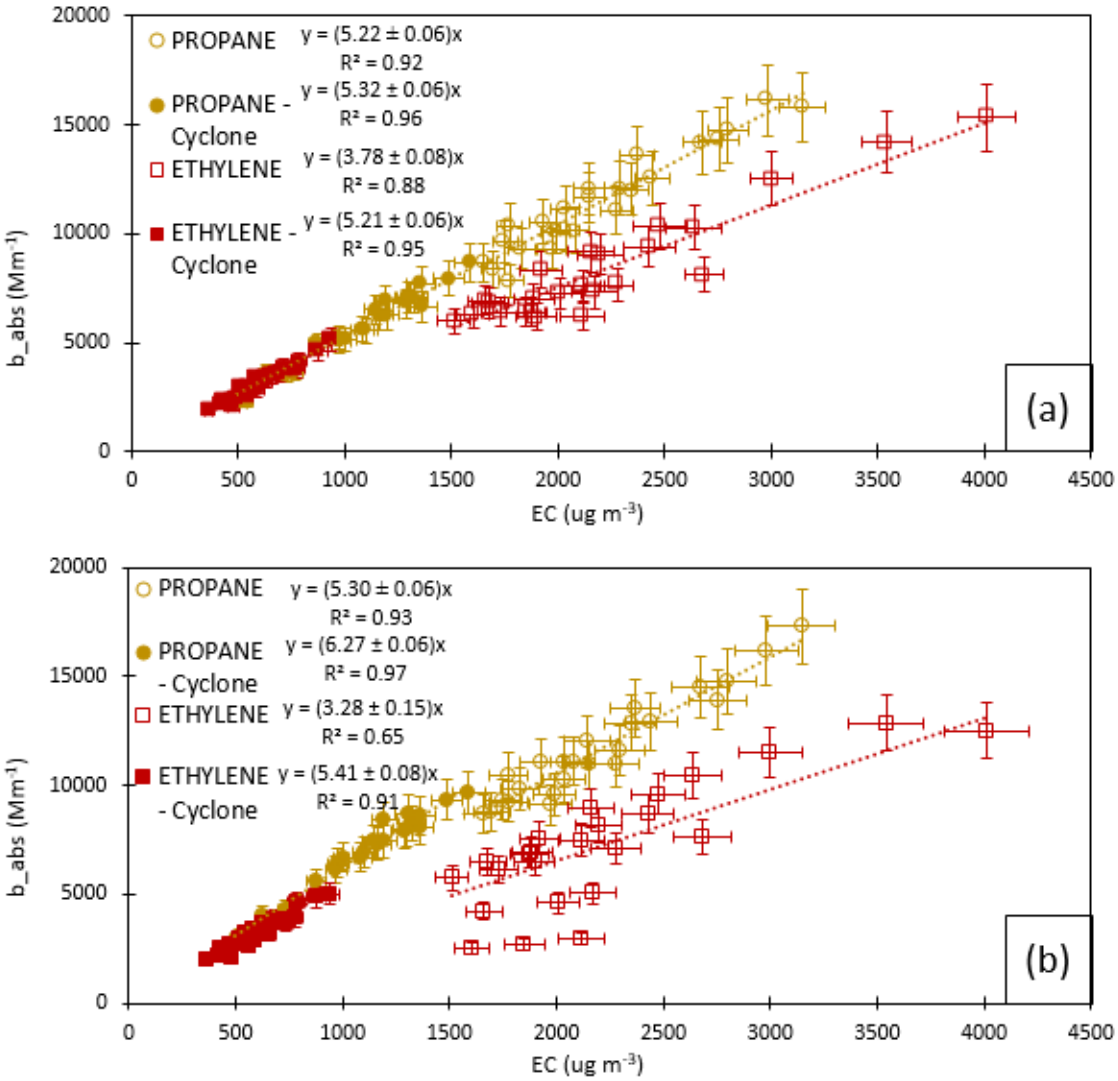

Figure 10: Absorption coefficient @850 nm measured by MWAA (a) and @870 nm measured by PAX (b) versus EC concentration. The slope of each fit corresponds to the Mass Absorption Coefficient.

MAC values are close to theoretical figures for soot (Bond and Bergstrom, 2006), for both the fuels and at all the wavelengths. IR values are similar to those obtained by Moallemi (2019) for propane exhaust. With both the fuels MAC values increase when super-micrometric particles were removed by the cyclone; propane-particles showed higher MAC values than ethylene ones.

In (Moallemi et al., 2019), only IR-MAC values for propane are reported, resulting slightly lower than values here quoted. This difference could depend on the techniques used to quantify the EC concentration: we measured EC values by thermal optical analysis while Moallemi (2019) reported BC concentration measured by LII.

Discrepancies between MAC values obtained by PAXs and MWAA, for the same experiment, are compatible with the differences of measured b_abs values: the latter are directly compared in Fig. 11, merging all the data collected by the two setups (i.e., with and without the cyclone) and for the two fuels. The agreement between the two instruments turned out within 25 % and 7 %, respectively without and with the cyclone.

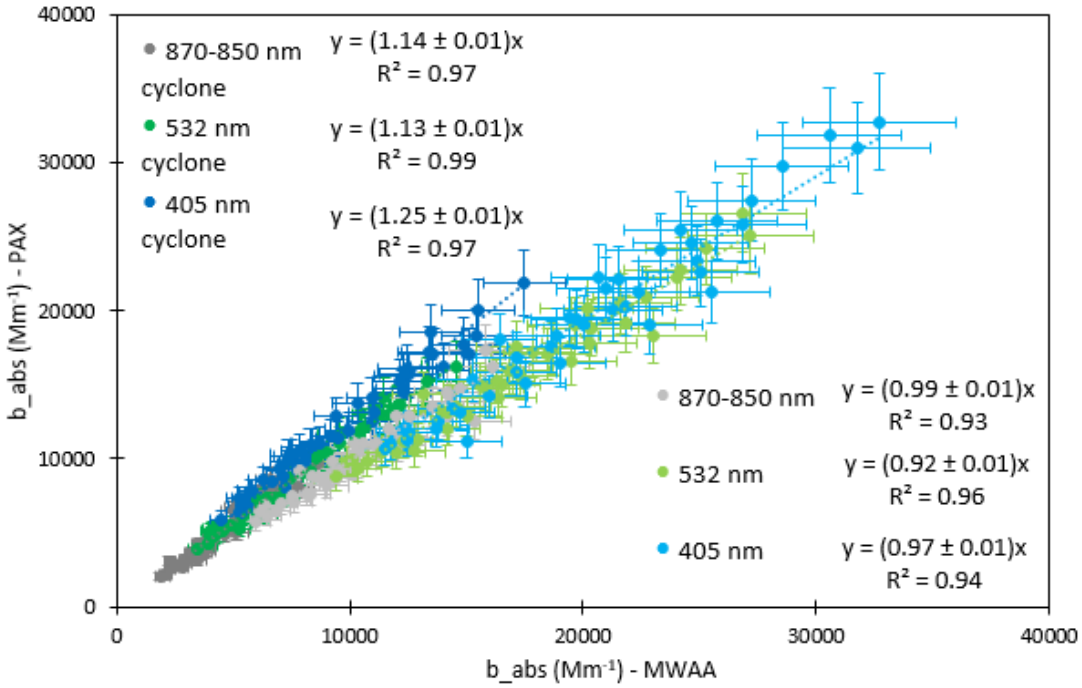

Figure 11: Correlation study between the absorption coefficient measured by PAX and MWAA. Colours of dots identify the wavelength of the analysis: grey refers to 870 nm, green to 532 nm and blue to 405 nm, with cyclone; light grey refers to 870 nm, light green to 532 nm and light blue to 405 nm; without cyclone.

In addition, the spectral dependence of the absorption coefficient b_abs, and consequently the Ångström Absorption Exponent (AAE, Moosmüller et al., 2011), can be calculated by the power-law:

$$b\_abs\ (\lambda) \approx \lambda^{-AAE}$$

where:

b_abs [Mm^{-1}]: absorption coefficient

λ [nm]: wavelength used for the analysis

AAE: Ångström Absorption Exponent.

The averages of the resulting AAEs values for the different experimental conditions are reported in Table 6 by fitting the data for the 3 and 5 available wavelengths in the case of PAXs and MWAA, respectively. Experimental determinations of the AAE had been reported in the literature as being dependent on aerosol chemical composition (Kirchstetter et al., 2004; Utry et al., 2013) and size and morphology (Lewis et al., 2008; Lack et al., 2012; Lack and Langridge, 2013; Filep et al., 2013; Utry et al., 2014 a). Particulate generated by fossil fuel combustion (i.e., Black Carbon) typically has AAE values close to 1.0 (Harrison et al., 2013, and references therein). The AAE values measured in this work for the MISG exhausts are generally close to 1.0 with higher figures for the cyclone-selected aerosol.

Table 6: AAE values obtained in different experimental conditions through the analysis of PAXs and MWAA raw data.

EXPERIMENTAL CONDITIONS	AAE - PAX	AAE - MWAA
PROPANE 70 to 85 mlpm - AIR 7 lpm	0.88 ± 0.06	0.92 ± 0.04
PROPANE 70 to 85 mlpm - AIR 8 lpm	0.92 ± 0.06	0.91 ± 0.05
PROPANE 70 to 85 mlpm - AIR 7 lpm - cyclone	0.98 ± 0.09	0.99 ± 0.10
PROPANE 70 to 85 mlpm - AIR 8 lpm - cyclone	1.05 ± 0.04	0.97 ± 0.09
ETHYLENE 118 to 144 mlpm - AIR 7 lpm	0.93 ± 0.28	0.84 ± 0.07
ETHYLENE 118 to 144 mlpm - AIR 8 lpm	0.76 ± 0.04	0.81 ± 0.06
ETHYLENE 118 to 144 mlpm - AIR 7 lpm - cyclone	1.40 ± 0.05	1.19 ± 0.09
ETHYLENE 118 to 144 mlpm - AIR 8 lpm - cyclone	1.39 ± 0.04	1.08 ± 0.05

Since the fit to 3 points could not be reliable, in the Supplementary (Table S.4) we reported the 2-wavelength calculations of the AAE for PAXs.

4. Conclusions

A Mini-Inverted Soot Generator (MISG) was coupled with an atmospheric simulation chamber (ChAMBRe) to compare the emissions when the burner is fed by two different fuels, ethylene, and propane. Different combustion conditions (i.e., air and fuel flow, global equivalence ratio) were characterized in terms of size distribution, particle and gas composition, optical properties, and EC concentration in the exhausts.

The MISG turned out to be a stable and reproducible soot particles source, suitable for experiments in atmospheric simulation chambers. In addition, properties of emitted soot particles can be slightly modulated by varying the combustion conditions i.e., tuning the global equivalence ratio and/or varying the fuel used for combustion.

With equal conditions, ethylene combustion produced particles with higher number concentration and smaller diameter than propane. Anyway, particles generated by both the fuels were larger than the typical exhausts of modern engines, such as aircraft and diesel vehicle engines, which emit ultrafine soot particles. Furthermore, it is noteworthy that ethylene combustion also generates super-micrometric aggregates. These are likely formed in the stagnation plane at the bottom part of the combustion cell. This information should be kept in mind when planning experiments, since super-aggregates, if not desired, could affect analysis.

The carbonaceous compounds produced by propane are generally characterized by higher EC to TC ratios than ethylene.

From the optical point of view, particles generated by propane turned out to be more light absorbing than those formed by ethylene, although burning conditions (in terms of global equivalence ratio) were the same. The values of the MAC parameter show a substantial agreement except for those retrieved from the data collected in the ethylene-no cyclone experiments. The latter resulted in lower MAC values, probably due to the presence of super-aggregates in the chamber.

This work opens to new and more complex experiments. Well-characterized soot particles could be used to investigate the effects that atmospheric parameters such as temperature and relative humidity can have on soot particles, and to study the interactions between soot particles and gaseous pollutants, solar radiation or bio-aerosol.

Author contribution

VV and DM prepared the experimental setup, performed all the experiments and the data analysis; DM, FP, SGD and PP designed and built ChAMBRe; MB designed and implemented the acquisition software; VV and DM prepared the article with contributions from the other authors.

Competing interests

The authors declare that they have no conflict of interest.

Special issue statement

This article is part of the special issue "Simulation chambers as tools in atmospheric research (AMT/ACP/GMD inter-journal SI)". It is not associated with a conference.

Acknowledgments

This project/work has received funding by the European Union's Horizon 2020 research and innovation program through the EUROCHAMP-2020 Infrastructure Activity under grant agreement No 730997.
This project/work has received funding by MIUR through the PON project PIR_00015 "Per ACTRIS IT" whose recipient is INFN.

References

Ackerman, A., Toon, O., Stevens, D., Heymsfield, A., Ramanathan, V., and Welton, E.: Reduction of tropical cloudiness by soot, Science, 288(5468), 1042–1047, doi:10.1126/science.288.5468.1042, 2000.

Anenberg, S. C., Horowitz, L. W., Tong, D. Q., and West, J. J.: An estimate of the global burden of anthropogenic ozone and fine particulate matter on premature human mortality using atmospheric modelling, Environ. Health Perspec., 118 (9):1189–95, doi:10.1289/ehp.0901220, 2010.

Baccolo, G., Nastasi, M., Massabò, D., Clason, C., Di Mauro, B., Di Stefano, E., Łokas, E., Prati, P., Previtali, E., Takeuchi, N., Delmonte, B., Maggi, V.: Artificial and natural radionuclides in cryoconite as tracers of supraglacial dynamics: Insights from the Morteratsch glacier (Swiss Alps), CATENA, 191:104577, 10.1016/j.catena.2020.104577, 2020.

Becker, K. H. (2006): Overview on the Development of Chambers for the Study of Atmospheric Chemical Processes, in: Environmental Simulation Chambers: Application to Atmospheric Chemical Processes, edited by: Barnes I. and Rudzinski K. J., Springer, Amsterdam, 1–26.

Bescond, A., Yon, J., Ouf, F. X., Roze, C., Coppalle, A., Parent, P., Ferry, D., and Laffon, C.: Soot optical properties determined by analyzing extinction spectra in the visible near-UV: Toward an optical speciation according to constituents and structure, J. Aerosol Sci. 101:118–32, doi:10.1016/j.jaerosci.2016.08.001, 2016.

Birch, M. E. and Cary, R. A.: Elemental carbon-based method for occupational monitoring of particulate diesel exhaust: methodology and exposure issues, Analyst, 121, 1183–1190, 1996.

Bischof, O. F., Weber, P., Bundke, U., Petzold, A., and Kiendler-Scharr, A.: Characterization of the Miniaturized Inverted Flame Burner as a Combustion Source to Generate a Nanoparticle Calibration Aerosol, Emission Contr. Sci. Technol. 6:37-46, DOI: 10.1007/s40825-019-00147-w, 2019.

Bond, T. C., and Bergstrom, R. W.: Light Absorption by Carbonaceous Particles: An Investigative Review, Aerosol Science and Technology, 40:1, 27-67, DOI: 10.1080/02786820500421521, 2006.

Bond T. C., Covert D. S., and Müller T.,: Truncation and Angular-Scattering Corrections for Absorbing Aerosol in the TSI 3563 Nephelometer, Aerosol Science and Technology, 43:9, 866-871, DOI: 10.1080/02786820902998373, 2009.

554 Bond, T. C., Doherty, S. J., Fahey, D. W., Forster, P. M., Berntsen, T., De Angelo, B. J., et al.: Bounding the
555 role of black carbon in the climate system: A scientific assessment, Journal of Geophysical Research
556 Atmospheres, 118(11), 5380–5552. https://doi.org/10.1002/jgrd.50171, 2013.

557 Caponi, L., Formenti, P., Massabó, D., Di Biagio, C., Cazaunau, M., Pangui, E., Chevaillier, S., Landrot, G.,
558 Andreae, M. O., Kandler, K., Piketh, S., Saeed, T., Seibert, D., Williams, E., Balkanski, Y., Prati, P., and
559 Doussin, J.-F.: Spectral- and size-resolved mass absorption efficiency of mineral dust aerosols in the shortwave
560 spectrum: a simulation chamber study, Atmos. Chem. Phys., 17, 7175–7191, https://doi.org/10.5194/acp-17-
561 7175-2017, 2017.

562 Cassee, F. R., Héroux, M. E., Gerlofs-Nijland, M. E., and Kelly, F. J.: Particulate matter beyond mass: Recent
563 health evidence on the role of fractions, chemical constituents and sources of emission, Inhalation Toxicology,
564 25(14), 802–812. https://doi.org/10.3109/08958378.2013.850127, 2013.

565 Chakrabarty, R. K., Moosmüller, H., Garro, M. A., and Stipe, C. B.: Observation of Superaggregates from a
566 Reversed Gravity Low-Sooting Flame, Aerosol Science and Technology, 46:1, i-iii, DOI:
567 10.1080/02786826.2011.608389, 2012.

568 Cross, E. S., Onasch, T. B., Ahern, A., Wrobel, W., Slowik, J. G., Olfert, J., Lack, D. A., Massoli, P., Cappa,
569 C. D., Schwarz, J. P., et al.: Soot particle studies-instrument inter-comparison-project overview, Aerosol Sci.
570 Technol., 44 (8):592–611. doi:10.1080/02786826.2010.482113, 2010.

571 Danelli, S. G., Brunoldi, M., Massabò, D., Parodi, F., Vernocchi, V., and Prati, P.: Comparative
572 characterization of the performance of bio-aerosol nebulizers in connection with atmospheric simulation
573 chambers, Atmos. Meas. Tech., 14, 4461–4470, https://doi.org/10.5194/amt-14-4461-2021, 2021.

574 Durdina, L., Lobo, P., Trueblood, M. B., Black, E. A., Achterberg, S., Hagen, D. E., Brem, B. T., and Wang,
575 J.: Response of real-time black carbon mass instruments to mini-CAST soot, Aerosol Sci. Technol. 50 (9):
576 906–18, doi: 10.1080/02786826.2016.1204423, 2016.

577 Filep, Á., Ajtai, T., Utry, N., Pintér, M. D., Nyilas, T., Takács, S., Máté, Z., Gelencsér, A., Hoffer, A.,
578 Schnaiter, M., Bozóki, Z., and Szabó, G.: Absorption spectrum of ambient aerosol and its correlation with size
579 distribution in specific atmospheric conditions after a red mud accident, Aerosol Air Qual. Res., 13, 49–59,
580 2013.

581 Finlayson-Pitts, B. J. and Pitts Jr., J. N.: Chemistry of the upper and lower atmosphere: Theory, experiments
582 and applications, Academic Press, San Diego, CA, 2000.

583 Gan, W. Q., Koehoorn, M., Davies, H. W., Demers, P. A., Tamburic, L., and Brauer, M.: Long-term exposure
584 to traffic-related air pollution and the risk of coronary heart disease hospitalization and mortality,
585 Environmental Health Perspectives, 119(4), 501–507, https://doi.org/10.1289/ehp.1002511, 2011.

586 Ghazi, R., and Olfert, J. S.: Coating mass dependence of soot aggregate restructuring due to coatings of oleic
587 acid and dioctyl sebacate, Aerosol Sci. Technol. 47 (2):192–200. doi:10.1080/02786826.2012.741273, 2013.

588 Ghazi, R., Tjong, H., Soewono, A., Rogak, S. N., and Olfert, J. S.: Mass, mobility, volatility, and morphology
589 of soot particles generated by a McKenna and inverted burner, Aerosol Sci. Technol. 47 (4):395–405.
590 doi:10.1080/02786826.2012.755259, 2013.

591 Harrison, R. M., Beddows, D. C. S., Jones A. M., Calvo A., Alves C., and Pio C.: An evaluation of some issues
592 regarding the use of aethalometers to measure woodsmoke concentrations, Atmos. Environ., 80, 540–548,
593 2013.

Henning, S., Ziese, M., Kiselev, A., Saathoff, H., Möhler, O., Mentel, T. F., Buchholz, A., Spindler, C., Michaud, V., Monier, M., et al.: Hygroscopic growth and droplet activation of soot particles: Uncoated, succinic or sulfuric acid coated, Atmos. Chem. Phys. 12 (10):4525–37.doi: 10.5194/acp-12-4525-2012, 2012.

Hu, D., Alfarra, M. R., Szpek, K., Langridge, J. M., Cotterell, M. I., Belcher, C., Rule, I., Liu, Z., Yu, C., Shao, Y., Voliotis, A., Du, M., Smith, B., Smallwood, G., Lobo, P., Liu, D., Haywood, J. M., Coe, H., and Allan, J. D.: Physical and chemical properties of black carbon and organic matter from different combustion and photochemical sources using aerodynamic aerosol classification, Atmos. Chem. Phys., 21, 16161–16182, https://doi.org/10.5194/acp-21-16161-2021, 2021.

Janssen, N., Gerlofs-Nijland, M., Lanki, T., Salonen, R., Cassee, F., Hoek, G., Fischer, P., Brunekreef, B., and Krzyzanowski, M.: Health effects of black carbon, Res. Rep., World Health Organization, Regional Office for Europe, Copenhagen, Denmark, 2012

Kazemimanesh, M., Moallemi, A., Thomson, K., Smallwood, G., Lobo, P., and Olfert, J. S.: A novel miniature inverted-flame burner for the generation of soot nanoparticles, Aerosol Science and Technology, 53 (2), 184-195, 10.1080/02786826.2018.1556774, 2019.

Kirchstetter, T. W., Novakok, T., and Hobbs, P. V.: Evidence that the spectral dependence of light absorption by aerosols is affected by organic carbon, J. Geophys. Res., 109, D21208, https://doi.org/10.1029/2004JD004999, 2004.

Kumar, N. K., Corbin, J. C., Bruns, E. A., Massabó, D., Slowik, J. G., Drinovec, L., Močnik, G., Prati, P., Vlachou, A., Baltensperger, U., Gysel, M., El-Haddad, I., and Prévôt, A. S. H.: Production of particulate brown carbon during atmospheric aging of residential wood-burning emissions, Atmos. Chem. Phys., 18, 17843–17861, https://doi.org/10.5194/acp-18-17843-2018, 2018.

Lack, D. A. and Langridge, J. M.: On the attribution of black and brown carbon light absorption using the Ångström exponent, Atmos. Chem. Phys., 13, 10535–10543, https://doi.org/10.5194/acp-13-10535-2013, 2013.

Lack, D. A., Langridge, J. M., Bahreini, R., Cappa, C. D., Middlebrook, A. M., and Schwarz, J. P.: Brown carbon and internal mixing in biomass burning particles, P. Natl. Acad. Sci. USA, 109, 14802–14807, 2012.

Lelieveld, J., Evans, J. S., Fnais, M., Giannadaki, D., and Pozzer, A.: The contribution of outdoor air pollution sources to premature mortality on a global scale, Nature 525 (7569):367–71. doi:10.1038/nature15371, 2015.

Lewis, K., Arnott, W. P., Moosmüller, H., and Wold, C. E.: Strong spectral variation of biomass smoke light absorption and single scattering albedo observed with a novel dual-wavelength photoacoustic instrument, J. Geophys. Res., 113, D16203, https://doi.org/10.1029/2007JD009699, 2008.

Mamakos, A., Khalek, I., Giannelli, R., and Spears, M.: Characterization of Combustion Aerosol Produced by a Mini-CAST and Treated in a Catalytic Stripper, Aerosol Science and Technology, 47:8, 927-936, DOI:10.1080/02786826.2013.802762, 2013.

Massabò, D., and Prati P.: An overview of optical and thermal methods for the characterization of carbonaceous aerosol, La Rivista del Nuovo Cimento, vo. 44:3, DOI: 10.1007/s40766-021-00017-8, 2021.

Massabò, D., Prati, P., Canepa, E., Bastianini, M., Van Eijk, A.M.J., Missamou, T., Piazzola, J.: Characterization of carbonaceous aerosols over the Northern Adriatic Sea in the JERICO-NEXT project framework, Atmospheric Environment, 228:117449, DOI: 10.1016/j.atmosenv.2020.117449, 2020.

633 Massabò, D., Altomari, A., Vernocchi, V., and Prati, P.: Two-wavelength thermal–optical determination of
634 light-absorbing carbon in atmospheric aerosols, Atmos. Meas. Tech., 12, 3173–3182,
635 https://doi.org/10.5194/amt-12-3173-2019, 2019.

636 Massabò, D., Danelli S. G., Brotto P., Comite A., Costa C., Di Cesare A., Doussin J. F., Ferraro F., Formenti
637 P., Gatta E., Negretti L., Oliva M., Parodi F., Vezzulli L., and Prati P.: ChAMBRe: a new atmospheric
638 simulation chamber for aerosol modelling and bioaerosol research, Atmos. Meas. Tech. 11, 5885-5900, 2018.

639 Massabò, D., Caponi, L., Bove, M. C., and Prati, P.: Brown carbon and thermal-optical analysis: a correction
640 based on optical multiwavelength apportionment of atmospheric aerosols, Atmos. Environ., 125, 119–125,
641 https://doi.org/10.1016/j.atmosenv.2015.11.011, 2016.

642 Massabò, D., Caponi, L., Bernardoni, V., Bove, M. C., Brotto, P., Calzolai, G., Cassola, F., Chiari, M., Fedi,
643 M. E., Fermo, P., Giannoni, M., Lucarelli, F., Nava, S., Piazzalunga, A., Valli, G., Vecchi, R., and Prati, P.:
644 Multi-wavelength optical determination of black and brown carbon in atmospheric aerosols, Atmos. Environ.,
645 108, 1–12, 2015.

646 Menon, S., Hansen, J., Nazarenko, L., and Luo, Y.: Climate effects of black carbon aerosols in China and
647 India, Science 297 (5590):2250–53. doi:10.1126/science1075159, 2002.

648 Moallemi, A., Kazemimanesh, M., Corbin, J. C., Thomson, K., Smallwood, G., Olfert, J. S., and Lobo, P.:
649 Characterization of black carbon particles generated by a propane-fueled miniature inverted soot generator,
650 Journal of Aerosol Science, 135, 46-57, 10.1016/j.jaerosci.2019.05.004, 2019.

651 Modini, R. L., Corbin, J. C., Brem, B. T., Irwin, M., Bertò, M., Pileci, R. E., Fetfatzis, P., Eleftheriadis, K.,
652 Henzing, B., Moerman, M. M., Liu, F., Müller, T., and Gysel-Beer, M.: Detailed characterization of the CAPS
653 single-scattering albedo monitor (CAPS PMssa) as a field-deployable instrument for measuring aerosol light
654 absorption with the extinction-minus-scattering method, Atmos. Meas. Tech., 14, 819–851,
655 https://doi.org/10.5194/amt-14-819-2021, 2021.

656 Moore R. H., Ziemba L. D., Dutcher D., Beyersdorf A. J., Chan K., Crumeyrolle S., Raymond T. M., Thornhill
657 K. L., Winstead E. L. and Anderson B. E.: Mapping the Operation of the Miniature Combustion Aerosol
658 Standard (Mini-CAST) Soot Generator, Aerosol Science and Technology, 48:5, 467-479, DOI:
659 10.1080/02786826.2014.890694, 2014.

660 Moosmüller, H., Chakrabarty, R.K., Ehlers, K.M., Arnott, W.P.: Absorption Ångström coefficient, brown
661 carbon, and aerosols: basic concepts, bulk matter, and spherical particles. Atmos. Chem. Phys. 11, 1217e1225,
662 2011.

663 Moschos, V., Gysel-Beer, M., Modini, R. L., Corbin, J. C., Massabò, D., Costa, C., Danelli, S. G., Vlachou,
664 A., Daellenbach, K. R., Szidat, S., Prati, P., Prévôt, A. S. H., Baltensperger, U., and El Haddad, I.: Source-
665 specific light absorption by carbonaceous components in the complex aerosol matrix from yearly filter-based
666 measurements, Atmos. Chem. Phys., 21, 12809–12833, https://doi.org/10.5194/acp-21-12809-2021, 2021.

667 Nemmar, A., Hoet, P.H.M., Vanquickenborne, B., Dinsdale, D., Thomeer, M., Hoylaerts, M.F., Vanbilloen,
668 H., Mortelmans, L., Nemery, B.: Passage of inhaled particles into the blood circulation in humans. Circulation
669 105, 411–414, https://doi.org/10.1161/hc0402.104118, 2002.

670 Nienow, A.M., and Roberts, J.T.: Heterogeneous Chemistry of Carbon Aerosols. Annual Review of Physical
671 Chemistry 57, 105–128, https://doi.org/10.1146/annurev.physchem.57.032905.104525, 2006.

672 NIOSH: Method 5040 Issue 3: Elemental Carbon (Diesel Exhaust). In NIOSH Manual of Analytical Methods.
673 National Institute of Occupational Safety and Health, Cincinnati, OH, 1999.

674 Nordmann, S., Birmili, W., Weinhold, K., Müller, K., Spindler, G., and Wiedensohler, A.: Measurements of
675 the mass absorption cross section of atmospheric soot particles using Raman spectroscopy, J. Geophys. Res.
676 Atmos., 118, 12,075–12,085, doi: 10.1002/2013JD020021, 2013.

677 Oberdörster, G., Oberdörster, E., Oberdörster, J.: Nanotoxicology: An Emerging Discipline Evolving from
678 Studies of Ultrafine Particles, Environmental Health Perspectives 113, 823–839.
679 https://doi.org/10.1289/ehp.7339, 2005.

680 Onasch, T. B., Trimborn, A., Fortner, E. C., Jayne, J. T., Kok, G. L., Williams, L. R., Davidovits, P. and
681 Worsnop, D. R.: Soot particle aerosol mass spectrometer: Development, validation, and initial application,
682 Aerosol Sci. Technol. 46 (7):804–17, doi:10.1080/02786826.2012, 663948, 2012.

683 Pagels, J., Khalizov, A. F., McMurry, P. H., and Zhang, R. Y.: Processing of soot by controlled sulphuric acid
684 and water condensation—Mass and mobility relationship, Aerosol Sci. Technol. 43 (7):629–4,
685 doi:10.1080/02786820902810685, 2009.

686 Petzold, A., Ogren, J. A., Fiebig,M., Laj, P., Li, S.-M., Baltensperger, U., Holzer-Popp, T.,Kinne, S.,
687 Pappalardo, G., Sugimoto, N.,Wehrli, C.,Wiedensohler, A., and Zhang, X.-Y.: Recommendations for
688 Reporting "Black Carbon", Measurements. Atmos. Chem. Phys., 13:8365–8379, 2013.

689 Petzold, A., Schloesser, H., Sheridan, P.J., Arnott, W.P., Ogren, J.A., Virkkula, A.: Evaluation of multiangle
690 absorption photometry for measuring aerosol light absorption, Aerosol Sci. Technol. 39 (1), 2005.

691 Petzold, A., and Schölinner, M.: Multi-angle absorption photometry—a new method for the measurement of
692 aerosol light absorption and atmospheric black carbon, Journal of Aerosol Science, 35, 421–441, 2004.

693 Pope, C.A. III, Burnett, R. T., Thun, M. J., Calle, E. E., Krewski, D., Ito, K., et al.: Lung Cancer,
694 Cardiopulmonary Mortality, and Long-term Exposure to Fine Particulate Air Pollution. J. Am. Med. Assoc.,
695 287(9):1132–41, 2002.

696 Quinn, P. K., Bates, T. S., Baum, E., Doubleday, N., Fiore, A. M., Flanner, M., et al.: Short-lived pollutants in
697 the Arctic: Their climate impact and possible mitigation strategies, Atmospheric Chemistry and Physics, 8(6),
698 1723–1735. https://doi.org/10.5194/acp-8-1723-2008, 2008.

699 Ramanathan, V., and G. Carmichael, G.: Global and regional climate changes due to black carbon, Nat. Geosci.
700 1 (4):221–27. doi:10.1038/ngeo156, 2008.

701 Saturno, J., Pöhlker, C., Massabò, D., Brito, J., Carbone, S., Cheng, Y., Chi, X., Ditas, F., Hrabě de Angelis,
702 I., Morán-Zuloaga, D., Pöhlker, M. L., Rizzo, L. V., Walter, D., Wang, Q., Artaxo, P., Prati, P., and Andreae,
703 M. O.: Comparison of different Aethalometer correction schemes and a reference multi-wavelength absorption
704 technique for ambient aerosol data, Atmos. Meas. Tech., 10, 2837–2850, https://doi.org/10.5194/amt-10-2837-
705 2017, 2017.

706 Scerri, M. M., Kandler, K., Weinbruch, S., Yubero, E., Galindo N., Prati, P., Caponi, L., and Massabò, D.:
707 Estimation of the contributions of the sources driving PM2.5 levels in a Central Mediterranean coastal town,
708 Chemosphere, 211, 465-481, https://doi.org/10.1016/j.chemosphere.2018.07.104, 2018.

709 Skiles, S.M., Flanner, M., Cook, J.M., Dumont, M., Painter, T.H.: Radiative forcing by light-absorbing
710 particles in snow. Nature Clim Change 8, 964–971. https://doi.org/10.1038/s41558-018-0296-5, 2018.

711 Stipe, C. B., Higgins, B. S., Lucas, D., Koshland, C. P., & Sawyer, R. F. Inverted co-flow diffusion flame for
712 producing soot, Review of Scientific Instruments, 76 (2), https://doi.org/10.1063/1.1851492, 2005.

713 Utry, N., Ajtai, T., Filep, Á., Dániel P. M., Hoffer, A., Bozoki, Z., and Szabó, G.: Mass specific optical
714 absorption coefficient of HULIS aerosol measured by a four-wavelength photoacoustic spectrometer at NIR,
715 VIS and UV wavelengths, Atmos. Environ., 69, 321–324, 2013.

716 Utry, N., Ajtai, T., Filep, Á., Pintér, M., Török, Zs., Bozóki, Z., and Szabó, G.: Correlations between absorption
717 Angström exponent (AAE) of wintertime ambient urban aerosol and its physical and chemical properties,
718 Atmos. Environ., 91, 52–59, 2014.

719 Utry, N., Ajtai, T.,Pinter, M., Bozóki, Z., and Szabó, G.: Wavelength-dependent optical absorption properties
720 of artificial and atmospheric aerosol measured by a multiwavelength photoacoustic spectrometer. Int. J.
721 Thermophys, 35 (12):2246–58. doi:10.1007/s10765-014-1746-6, 2014

722 von der Weiden, S.-L., Drewnick, F., and Borrmann, S.: Particle Loss Calculator – a new software tool for the
723 assessment of the performance of aerosol inlet systems, Atmos. Meas. Tech., 2, 479–494,
724 https://doi.org/10.5194/amt-2-479-2009, 2009.

725 Weijer, E. P., Schaap, M., Nguyen, L., Matthijsen, J., Denier van der Gon, H. A. C., et al.: Anthropogenic and
726 Natural Constituents in Particulate Matter in the Netherlands, Atmos. Chem. Phys., 11:2281–2294, 2011.

727 Zhang, R., Khalizov, A. F., Pagels, J., Zhang, D., Xue, H., and McMurry, P. H.: Variability in morphology,
728 hygroscopicity, and optical properties of soot aerosols during atmospheric processing, Proc. Natl. Acad. Sci.
729 USA 105 (30):10291–96. doi:10.1073/pnas.0804860105, 2008.